Lateral-Structure Single-Crystal Hybrid Perovskite Solar Cells via Piezoelectric Poling

*Qingfeng Dong, Jingfeng Song, Yanjun Fang, Yuchuan Shao, Stephen Ducharme, and Jinsong Huang**

The efficiencies of solution-processed organometal trihalide perovskite (OTP) solar cells are now rivaling that of single-crystal silicon solar cells,[1–22] but they are built on transparent electrodes which constitute for a major part of the cost of these devices despite OTP materials are cheap.[23,24] The development of OTP devices with a lateral, or coplanar, structure enables dramatic cost reduce of OTP solar cells by eliminating expensive transparent electrodes.[23,24] It also enhances the light harvesting efficiency because of eliminated loss of light by the transparent electrodes through absorption, reflection, and scattering, and allows light trapping using a simple texture structure as established in single-crystal silicon solar cells.[25,26] In addition, the configuration of lateral-structure solar cells facilitates vertical stacking of subcells with complimentary absorption spectra to capture sun light with a wider wavelength range (patent pending). Nevertheless, the carrier diffusion lengths in the polycrystalline OPTs are still too small to yield efficient lateral-structure OPT solar cells due to the strong scattering of charge carriers at the grain boundaries.[24,27] The highest power conversion efficiency (PCE) obtained with polycrystalline lateral-structure OTPs was below 0.1%.[27] Our recent discovery of very long carrier diffusion length > 175 micrometers (μm) in single-crystalline methylammonium lead triiodide ($MAPbI_3$) provides a new opportunity to revisit the lateral-structure device as a means to achieving high efficiency in OTP solar cells.[28]

Here we show that hybrid perovskite solar cells can be fabricated with a lateral structure using OTP single crystals, which eliminates the need for transparent electrodes. Replacing the polycrystalline OTP thin films with the single crystals yields an efficiency enhancement of 44 folds, enabled by much longer carrier diffusion lengths in the OTP single crystals which allow the charges to be efficiently collected along the lateral direction. Strong piezoelectric effect is observed in OTP single crystals, which enables the poling of the single crystals under nonuniform electric field. The strain-generated grain boundaries provide paths for the ion migration to form a *p–i–n* structure.

The photovoltaic devices had a lateral structure of electrode/$MAPbI_3$/electrode,[24] and they were fabricated by depositing two parallel electrode on one facet of the $MAPbI_3$ single crystals (MSCs). The electrode materials could be varied conductive materials such as carbon,[29] gold (Au),[24] etc. which do not react with OTP. Devices studied in this report use gold as electrode because of the higher stability of Au on perovskite during different measurement, which could well demonstrate the concept of lateral-structure single crystal solar cell. For the devices studied in this report with a structure of Au/$MAPbI_3$/Au, there was negligible photovoltaic effect for the as-prepared devices with the symmetrical Au electrodes. It has been established previously that an electrical poling is required to break the electrode symmetry so that a *p–i–n* structure, induced by ion migration and self-doping, can be formed.[24,27–30] Nevertheless, as reported in the previous work,[24] the grain boundaries might be the dominating path for ion migration under the applied field in the OTP polycrystalline thin films, because the energy barrier for ion migration within the grain boundaries is half as large as compared to in the bulk. This imposes a fundamental challenge for the poling of single-crystal OTPs devices because of the absence of grain boundaries in them.[24]

Interestingly, we discovered the OTP single crystals showed strong piezoelectric effect. The grain boundaries caused by the crystal facture, which is caused by the piezoelectric poling, in single crystal enabled ion migration, which resulted in the *p–i–n* structure formation. Piezoelectric effect is a reversible process exhibiting both the direct piezoelectric effect (electrical charges generated by an applied mechanical force) and reverse piezoelectric effect (mechanical strain response to an applied electrical field)[31,32] Previous work of Coll et al. has studied the local piezoelectric response of polycrystalline OTP film with piezoresponse force microscopy (PFM) measurement.[33] Nevertheless, study of the piezoelectric response from a large size single-crystal device is needed for direct evidence and quantitative measurement of the piezoelectric properties of OTP crystals, since the local PFM study on polycrystalline film could be limited by the inaccurate estimation of tip contact area and other artifacts[34] coming from surface topography and crystal orientation.[35–37] To verify the piezoelectric effect, we fabricated a single-crystal device with a different vertical structure, i.e., a $MAPbI_3$ single crystal sandwiched by two electrodes on

Dr. Q. Dong, Dr. Y. Fang, Y. Shao
Department of Mechanical and Materials Engineering
University of Nebraska-Lincoln
Lincoln, NE 68588-0656, USA
Dr. Q. Dong, J. Song, Dr. Y. Fang, Y. Shao, S. Ducharme, Prof. J. Huang
Nebraska Center for Materials and Nanoscience
University of Nebraska-Lincoln
Lincoln, NE 68588-0299, USA
E-mail: jhuang2@unl.edu
J. Song, Prof. S. Ducharme
Department of Physics and Astronomy
Nebraska Center for Materials and Nanoscience
University of Nebraska-Lincoln
Lincoln, NE 68588-0299, USA

DOI: 10.1002/adma.201505244

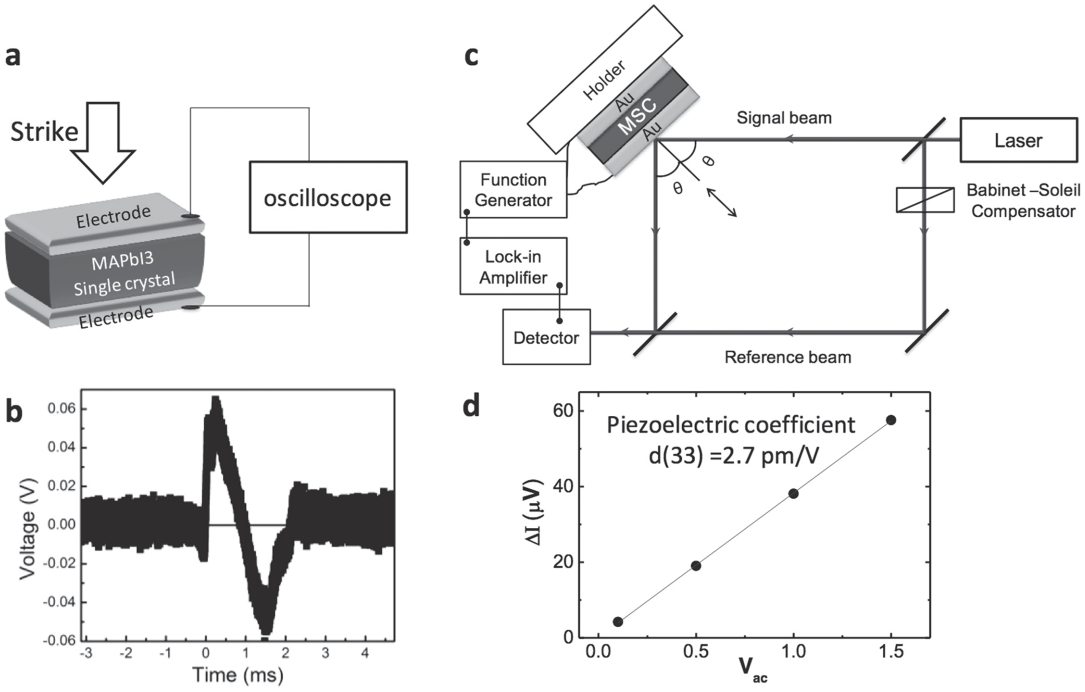

Figure 1. Piezoelectric measurement of $MAPbI_3$ single crystals. a) Set up and b) voltage output over time recorded by oscilloscope by striking the single crystal gently. The single crystal device in this study had two electrodes deposited on parallel surfaces of the crystal. c) Set up of the high-resolution Mach–Zehnder interferometer for the piezoelectric coefficient measurements. d) Plot of the intensity modulation ΔI versus amplitude of the 1 kHz ac electric field applied across the crystal. The crystal was poled under 0.1 V μm^{-1} electric field across the paralleled electrodes for 5 min then turned off, while the small sinusoidal ac voltage at frequency of 1 kHz acted as the piezoelectric driving field.

two parallel facets of the crystals as shown in **Figure 1**a. This device showed positive and negative voltage pulse when it was squeezed and released by simple striking it gently (Figure 1b), providing a direct evidence for the presence of piezoelectric effect in $MAPbI_3$ single crystals.[31,32] We did not see such a phenomenon in the reference device based on $MAPbI_3$ polycrystalline thin film with the same test condition as single crystal devices. This possibly due to the random distribution of grain orientation in polycrystalline films, which indicates a single crystal is critical for the piezoelectric property measurement. As the laser interferometry method has been proved to be reliable and high in accuracy from previous piezoelectric coefficient measurement,[38] for our single crystal sample, a high-resolution Mach–Zehnder interferometer was adopted to record the crystal shape change under an applied alternating electric field in the range of 1–20 kV m^{-1} for piezoelectric coefficient measurements, with the setup shown in Figure 1c.[39] The measured piezoelectric coefficient (d_{33}) is 2.7 pm V^{-1} along [001] direction (Figure 1d), with no observable electrostriction effect for the $MAPbI_3$ single crystals.

Figure 2a shows an image of the lateral-structure $MAPbI_3$ single-crystal device. Since the electric field applied in the lateral-structure devices was nonuniform, with a higher field close to the electrode region as illustrated in Figure 2b, the field-induced strain was highly nonuniform. The nonuniform crystal strain in the lateral-structure devices caused a crystal-plane displacement when the applied electric field reached 1 Vμm^{-1}, as shown in Figure 2c and d. A dense array of stripes appeared upon the application of a poling bias of 50 V on Au electrodes (Figure 2e) and disappeared after turning off the applied poling bias (Figure 2f). During the poling of the $MAPbI_3$ single crystal under a relatively high poling field of 1 Vμm^{-1}, two sets of parallel strip lines showed up on the surface of the $MAPbI_3$ single crystal, which is likely formed by the slipping of the weakly bonded (100) planes with respect to each other to relieve the accumulated strain. Although the crystal recovered its shape in macroscopic scale after turning off the applied bias, there should be defects generated in the crystal during the poling process. The slipping-generated interfaces/grain boundaries and dislocation lines are proposed to provide a high-speed channel for the ion migration under the electric field, resulting in the formation *p–i–n* structure by the ion doping.[24] The formation of *p–i–n* junction after poling in single crystals can be verified by the *J–V* characteristics of diodes (rectification) in the dark. As shown in Figure S1 in the Supporting Information, the devices showed significantly improved rectification property after poling compared with the symmetric *J–V* curve before poling, which indicates the formation of *p–i–n* structure.

The *p–i–n* or *n–i–p* doping can be tuned by changing the poling direction. The formation of reversible *p–i–n* structure was induced by ion drift under applied electric field in the perovskite layer as described in our previous work.[24,27] The direction of ion migration can be controlled by the direction of applied electric field for the formation of *p–i–n* or *n–i–p* doping. **Figure 3**a shows the typical switchable photovoltaic behavior of a lateral Au/MSC/Au device. The open-circuit voltage (V_{OC}) direction was in agreement with the poling bias direction. The much longer diffusion length in the $MAPbI_3$ single crystals

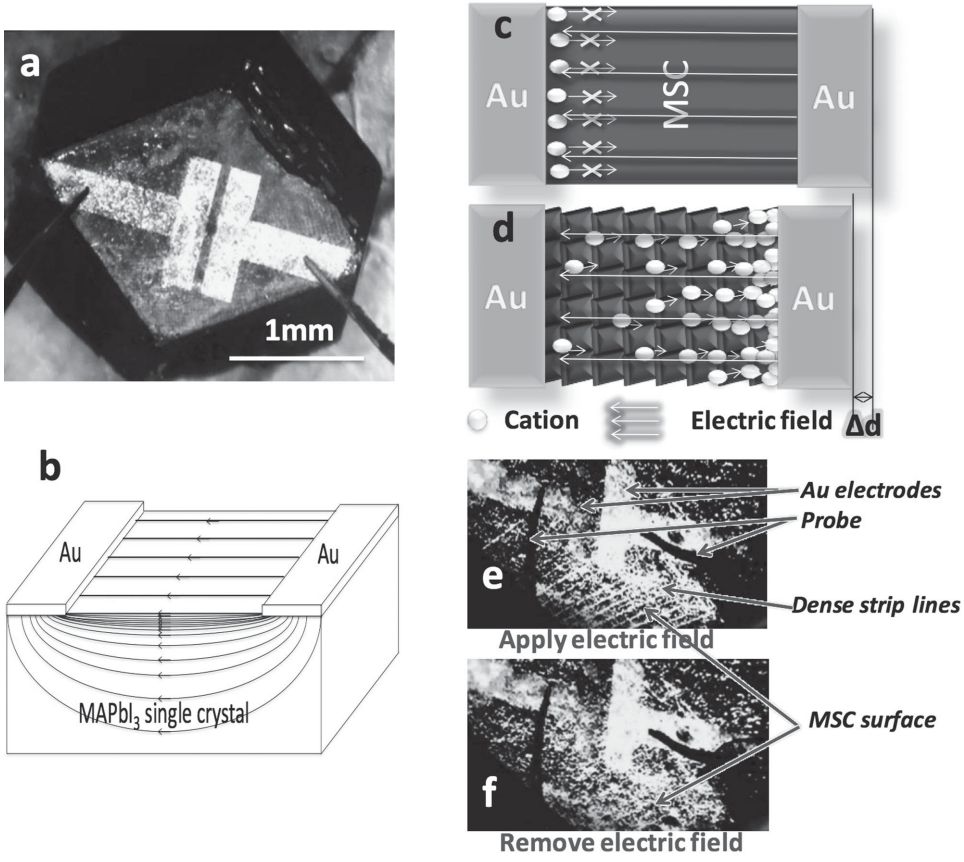

Figure 2. Piezoelectric poling of $MAPbI_3$ lateral structure single-crystal solar cells. a) An image of $MAPbI_3$ lateral structure single-crystal device. b) Illustration of the poling electric field distribution in top surface and cross-section of a lateral single crystal device. c,d) Scheme of electromechanical strain generated grain boundaries and irons migration in $MAPbI_3$ single crystals. e,f) Images of $MAPbI_3$ lateral structure single-crystal devices with and without applied electric field.

than in polycrystalline thin films resulted in much more efficient charge collection. Figure 3b shows the photocurrents of a $MAPbI_3$ lateral-structure single-crystal device and a lateral-structure polycrystalline thin film device with the same electrode spacing of 50 μm under white illumination with an intensity of 25 mW cm^{-2} (0.25 sun). Polycrystalline thin film and device was fabricated on glass substrate by the interdiffusion method reported in our previous work and the film was continues and had full coverage,[24,27] The $MAPbI_3$ lateral-structure single crystal device showed a J_{SC} of 2.28 mA cm^{-2} (Figure 3b), which is about 33 times larger than that of the lateral-structure polycryalline devices. And the V_{OC} increased significantly from 0.61 V for the thin-film device to 0.82 V for the single crystal device. The normalized EQE curve of MSC lateral structure device shown in Figure 3c shows a significant extension of the cutoff to ≈850 nm, in contrast to the cutoff of 800 nm from $MAPbI_3$ thin film devices, which is in consistent with the result in vertical-structure single-crystal device.[28] It is caused by the below bandgap absorption which only becomes significant in the very thick single crystals. It can potentially boost the J_{SC} upper limit of the $MAPbI_3$ single crystal based solar cells.

The $V_{OC,}$ short circuit current density (J_{SC}) and PCE of the $MAPbI_3$ lateral-structure single-crystal device is strongly temperature dependent. As shown in Figure 3d, a highest PCE of 5.36 % is reached at 170 K for the lateral-structure single crystal device, with a high J_{SC} comparable to the best thin-film solar cells under the same light intensity. The J_{SC} increased when the temperature was reduced from 250 to 170 K, which should be ascribed to the enhanced carrier mobility and reduced charge recombination rate at lower temperatures. There was a sharp transition of J_{SC} variation trend at 170 K, which corresponds to crystal phase transformation from tetragonal to orthorhombic.[40,41] The J_{SC} decreased at further reduced temperature from 170 to 77 K. The different trends of J_{SC} variation with temperature across the phase transformation temperature may be related to the exciton dissociation efficiency. It was reported that exciton screening effect by collective orientational motion of the organic cations in the tetragonal phase leads to the easy dissociation of the excitons into free carriers.[40] In the orthorhombic phase, the motion of organic cations is restricted and bound-exciton forms,[40] resulting in the decreased J_{SC} at lower temperature. However more study is needed to find out the exact mechanism. The V_{OC} of lateral-structure single-crystal device reached 0.8–0.9 V, which is the same as previously reported vertical-structure polycrystalline devices without a hole transport layer.[29,42] Optimization of the electrode material work function, as well as incorporation of electron/hole transport layers to achieve a better energy-level alignment should

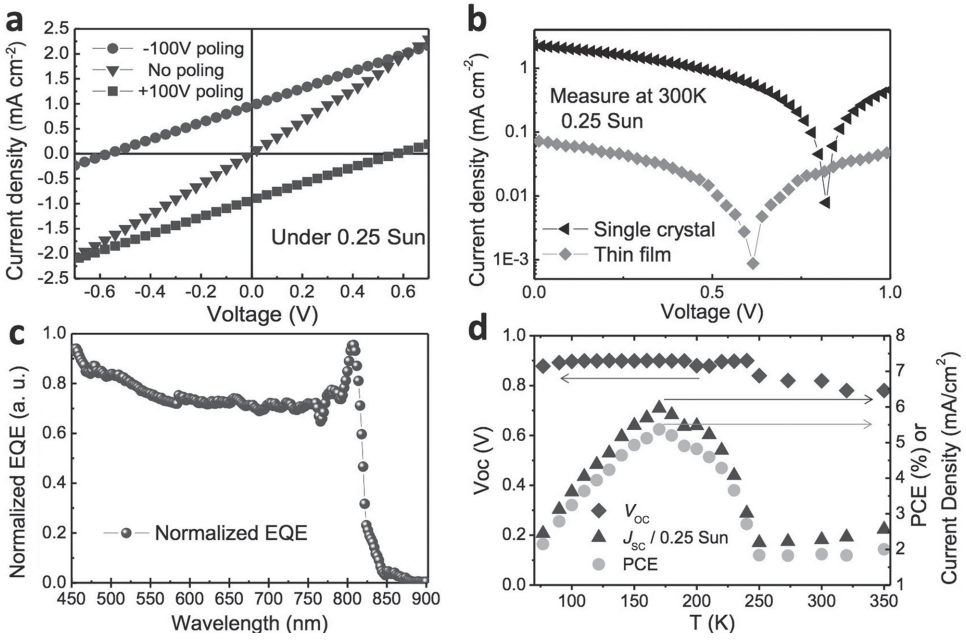

Figure 3. Device performance of $MAPbI_3$ single-crystal solar cells. a) Switchable photovoltaic effect of a $MAPbI_3$ lateral-structure single-crystal solar cell with positive and negative poling. b) Photocurrents of the $MAPbI_3$ single crystals and polycrystalline thin films with a same electrode spacing of 50 μm under 25 mW cm^{-2} illumination at room temperature. c) EQE curve and d) temperature-dependent device performance of the $MAPbI_3$ single-crystal solar cell.

further increase the PCE and V_{OC} of the lateral-structure single-crystal solar cells. The PCE of the lateral-structure device was 1.88 % at room temperature, representing a 44-fold enhancement compared to the thin-film lateral-structure polycrystalline devices.[27] The lateral-structure single-crystal devices showed a small photocurrent hysteresis with changed *J*–*V* scan rate and scan directions as shown in Figure S2 in the Supporting Information. The scan rate-dependent hysteresis test was in time scale of minutes that is consistent with the stabilized photocurrent output of the device at the maximum power point (J_{MPP}). Figure S2b in the Supporting Information shows the J_{MPP} for a continuous testing over 1 h. The value of J_{MPP} rose to a peak value of approximately 1 mA cm^{-2} in 2 min under 0.25 sun illumination at room temperature, and then reached a stable output of ≈1 mA cm^{-2} again after experiencing a dip. The variation of photocurrent output can be possibly caused by the combination of trap filling process and ions redistribution driven by the photovoltage.[43]

Photocurrent scanning was conducted on a $MAPbI_3$ lateral-structure single-crystal device with 70 μm electrodes spacing to evaluate the charge collection length in these single crystals.[44] The much longer carrier diffusion length of the single crystal principally allows the using of focused laser beam instead of electron beam to locally genera the charges.[38] The device was loaded onto a programmable *X*–*Y* position stage, and was illuminated by a focused 632 nm laser beam with a focused light spot size of approximately 1 μm on the MSC surface (**Figure 4**a).[44] Figure 4b shows the relative photocurrent intensity by scanning

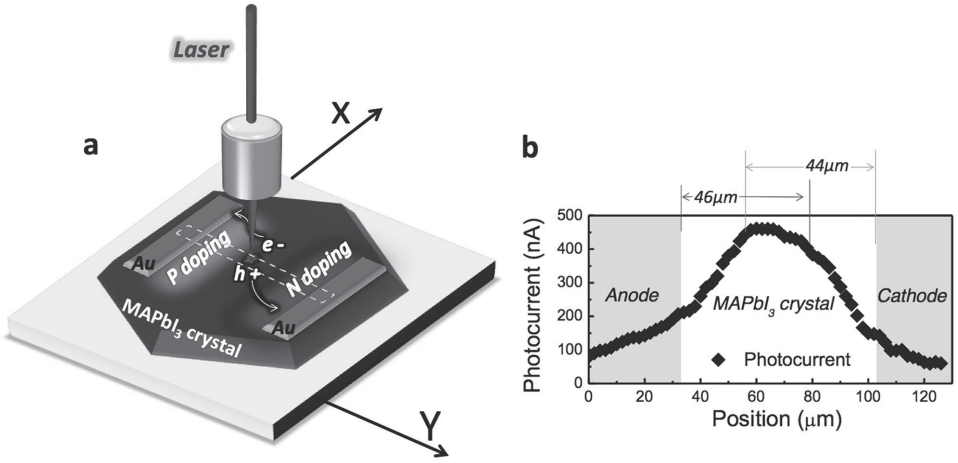

Figure 4. Photocurrent scanning across a $MAPbI_3$ lateral structure single-crystal device. a) Setup of photocurrent scanning and b) photocurrent scanning result measured as a function of the beam position scanning from anode to cathode of the MSC device.

laser spot across anode to cathode of the lateral-structure device. There is an increasing photocurrent toward the center, while there is a relatively flat region of photocurrent generated close to the center, where the photo-generated electrons and holes should be most efficiently collected by the cathode and anode with a good balance. We speculated a comparable electron or hole diffusion length of approximately 45 μm in the $MAPbI_3$ single crystals reported here.[45,46] The carrier diffusion length is smaller than previously reported because there are grain boundaries generated during electrical poling process which induce more defect than the single crystal before poling. However, the carrier diffusion length in poled single crystal is still much longer than polycrystalline thin films, so the charges can be collected in lateral direction. The poling-induced crystal damage should be the main limitation of device performance for lateral device, but at the same time it also indicates a way to further increase the efficiency of lateral-structured solar cell by minimize the damage to the crystal. For example, one can develop new method to achieve *p–i–n* structure by direct doping of OTP single crystal below the two electrodes, similar to the method of doping in silicon transistor fabrication. The PCE of 1.88% for lateral-structure single crystal solar cell at room temperature is still lower than efficiencies commonly reported for vertical devices, but it is promising considering fact that the first perovskite solar cell was not efficiency either.

In summary, the lateral-structure devices made from solution-grown OTP single crystals open a new route to fabrication of efficient low-cost solar cells with a very simple device structure of metal/crystal/metal. This innovation eliminates the need for more expensive and efficiency-reducing transparent electrodes. The transparent electrode-free device structure also provides a new paradigm to enhance the light absorption efficiency in active layer. We speculate that intentionally doped perovskite layers at the cathode and anode sides, rather than those formed by electrical poling, should further increase the PCE of these lateral-structure single-crystal structure devices, because it will preserve the long carrier diffusion length of the single crystals. The demonstration of efficient lateral perovskite solar cells allows new design of tandem devices by integrating perovskite devices with other types of solar cells.

Experimental Section

Device Fabrication and Characterization: Single crystals were prepared by slowly cooling down the supersaturated $MAPbI_3$ precursor solution from 110 to 60 °C with a cooling rate of approximately 0.1–0.5 °C h^{-1}. The precursor solution was prepared as previously reported.[28] The resulted crystals were separated from mother solution, and then washed with diethyl ether and isopropyl alcohol. The lateral-structure single-crystal devices were fabricated by depositing parallel Au bar electrodes (75 nm thick) with varied spacing on one facet of the MSCs by vacuum thermal evaporation with shadow masks. For *J–V* test, both side of gap spacing on top crystal surface was covered by metal electrodes as a function of mask for accurate definition of device working area. The working area of MSC lateral solar cell was 50 μm × 1000 μm. Then MSCs with Au electrodes were poled by applying 50–200 V bias for varied duration. The poling process and the following measurements on lateral-structure solar cells were conducted in a probe station chamber under a vacuum of 10^{-5} Pa, under white light (25 mW cm^{-2}) through a quartz window. The temperature was decreased to 77 K and the temperature-dependent device performance was measured with slowly increased temperature at 350 K. N_2 atmosphere was used to protect the sample from moisture during current mapping measurement.

Piezoelectric Coefficient Measurement: Two paralleled crystal facets were chosen to deposit Au electrode (75 nm) for the measurement. A collimated He–Ne laser beam (wavelength of 632 nm) with a spot size of ≈2 mm came in perpendicular onto the crystal top (001) surface. The bottom crystal plane was glued to the sample holder which is fixed, while the top surface of the crystal could move freely. The thickness change under applied electric field was measured by the interferometer.

Supporting Information

Supporting Information is available from the Wiley Online Library or from the author.

Acknowledgements

Q.D. and J.S. contributed equally to this work. The authors thank the financial support from National Science Foundation (DMR1505535 and ECCS-1348272).

Received: October 24, 2015
Revised: December 24, 2015
Published online: February 2, 2016

[1] J. Burschka, N. Pellet, S.-J. Moon, R. Humphry-Baker, P. Gao, M. K. Nazeeruddin, M. Grätzel, *Nature* **2013**, *499*, 316.
[2] S. D. Stranks, G. E. Eperon, G. Grancini, C. Menelaou, M. J. Alcocer, T. Leijtens, L. M. Herz, A. Petrozza, H. J. Snaith, *Science* **2013**, *342*, 341.
[3] M. M. Lee, J. Teuscher, T. Miyasaka, T. N. Murakami, H. J. Snaith, *Science* **2012**, *338*, 643.
[4] A. Kojima, K. Teshima, Y. Shirai, T. Miyasaka, *J. Am. Chem. Soc.* **2009**, *131*, 6050.
[5] Z. Xiao, C. Bi, Y. Shao, Q. Dong, Q. Wang, Y. Yuan, C. Wang, Y. Gao, J. Huang, *Energ. Environ. Sci.* **2014**, *7*, 2619.
[6] N. J. Jeon, J. H. Noh, W. S. Yang, Y. C. Kim, S. Ryu, J. Seo, S. I. Seok, *Nature* **2015**, *517*, 476.
[7] H. Zhou, Q. Chen, G. Li, S. Luo, T.-b. Song, H.-S. Duan, Z. Hong, J. You, Y. Liu, Y. Yang, *Science* **2014**, *345*, 542.
[8] N. J. Jeon, J. H. Noh, Y. C. Kim, W. S. Yang, S. Ryu, S. I. Seok, *Nat. Mater.* **2014**, *13*, 897.
[9] M. Grätzel, *Nat. Mater.* **2014**, *13*, 838.
[10] M. A. Green, K. Emery, Y. Hishikawa, W. Warta, E. D. Dunlop, *Prog. Photovoltaics: Res. Appl.* **2015**, *23*, 1.
[11] S. D. Stranks, H. J. Snaith, *Nat. Nanotechnol.* **2015**, *10*, 391.
[12] J.-H. Im, I.-H. Jang, N. Pellet, M. Grätzel, N.-G. Park, *Nat. Nanotechnol.* **2014**, *9*, 927.
[13] W. S. Yang, J. H. Noh, N. J. Jeon, Y. C. Kim, S. Ryu, J. Seo, S. I. Seok, *Science* **2015**, *348*, 1234.
[14] A. Buin, R. Comin, J. Xu, A. H. Ip, E. H. Sargent, *Chem. Mater.* **2015**, *27*, 4405.
[15] S. D. Stranks, S. M. Wood, K. Wojciechowski, F. Deschler, M. Saliba, H. Khandelwal, J. B. Patel, S. Elston, L. M. Herz, M. B. Johnston, *Nano Lett.* **2015**, *27*, 4405.
[16] W. Zhang, M. Saliba, D. T. Moore, S. K. Pathak, M. T. Hörantner, T. Stergiopoulos, S. D. Stranks, G. E. Eperon, J. A. Alexander-Webber, A. Abate, *Nat. Commun.* **2015**, *6*, 6412.
[17] Q. Lin, A. Armin, R. C. R. Nagiri, P. L. Burn, P. Meredith, *Nat. Photonics* **2014**, *9*, 106.

[18] J. Shi, X. Xu, D. Li, Q. Meng, *Small* **2015**, *11*, 2472.
[19] M. A. Green, A. Ho-Baillie, H. J. Snaith, *Nat. Photonics* **2014**, *8*, 506.
[20] F. Hao, C. C. Stoumpos, D. H. Cao, R. P. Chang, M. G. Kanatzidis, *Nat. Photonics* **2014**, *8*, 489.
[21] M. R. Filip, G. E. Eperon, H. J. Snaith, F. Giustino, *Nat Commun.* **2014**, *5*, 5757.
[22] Q. Dong, Y. Yuan, Y. Shao, Y. Fang, Q. Wang, J. Huang, *Energ. Environ. Sci.* **2015**, *8*, 2464.
[23] B. Azzopardi, C. J. Emmott, A. Urbina, F. C. Krebs, J. Mutale, J. Nelson, *Energ. Environ. Sci.* **2011**, *4*, 3741.
[24] Z. Xiao, Y. Yuan, Y. Shao, Q. Wang, Q. Dong, C. Bi, P. Sharma, A. Gruverman, J. Huang, *Nat. Mater.* **2015**, *14*, 193.
[25] P. Campbell, M. A. Green, *J. Appl. Phys.* **1987**, *62*, 243.
[26] H. Savin, P. Repo, G. von Gastrow, P. Ortega, E. Calle, M. Garín, R. Alcubilla, *Nat. Nanotechnol.* **2015**, *10*, 624.
[27] Y. Yuan, J. Chae, Y. Shao, Q. Wang, Z. Xiao, A. Centrone, J. Huang, *Adv. Energy Mater.* **2015**, *5*, 1500615.
[28] Q. Dong, Y. Fang, Y. Shao, P. Mulligan, J. Qiu, L. Cao, J. Huang, *Science* **2015**, *347*, 967.
[29] A. Mei, X. Li, L. Liu, Z. Ku, T. Liu, Y. Rong, M. Xu, M. Hu, J. Chen, Y. Yang, *Science* **2014**, *345*, 295.
[30] Q. Wang, X. Liu, Y. Shao, Y. Gao, J. Huang, *Appl. Phys. Lett.* **2014**, *105*, 163508.
[31] D.-I. E. G. Gautschi, *Piezoelectric Sensors*, Springer, New York, **2002**.
[32] A. Arnau, D. Soares, *Piezoelectric Transducers and Applications*, Springer, New York, **2008**, pp. 1.
[33] M. Coll, A. Gomez, E. Mas-Marza, O. Almora, G. Garcia-Belmonte, M. Campoy-Quiles, J. Bisquert, *J. Phys. Chem. Lett.* **2015**, *6*, 1408.
[34] A. Labuda, R. Proksch, *Appl. Phys. Lett.* **2015**, *106*, 253103.
[35] N. Balke, P. Maksymovych, S. Jesse, I. I. Kravchenko, Q. Li, S. V. Kalinin, *ACS Nano* **2014**, *8*, 10229.
[36] S. V. Kalinin, A. Kumar, N. Balke, M. L. McCorkle, S. Guo, T. M. Arruda, S. Jesse, *Adv. Mater.Proc.* **2011**, *169*.
[37] S. V. Kalinin, S. Jesse, A. Tselev, A. P. Baddorf, N. Balke, *Acs Nano* **2011**, *5*, 5683.
[38] J.-M. Liu, B. Pan, H. Chan, S. Zhu, Y. Zhu, Z. Liu, *Mater. Chem. Phys.* **2002**, *75*, 12.
[39] A. Bune, C. Zhu, S. Ducharme, L. Blinov, V. Fridkin, S. Palto, N. Petukhova, S. Yudin, *J. Appl. Phys.* **1999**, *85*, 7869.
[40] H. H. Fang, R. Raissa, M. Abdu-Aguye, S. Adjokatse, G. R. Blake, J. Even, M. A. Loi, *Adv. Funct. Mater.* **2015**, *25*, 2378.
[41] Y. Kawamura, H. Mashiyama, K. Hasebe, *J. Phys. Soc. Jpn.* **2002**, *71*, 1694.
[42] Z. Wei, H. Chen, K. Yan, S. Yang, *Angew. Chem.* **2014**, *126*, 13455.
[43] Y. Deng, Z. Xiao, J. Huang, *Adv. Energy Mater.* **2015**, *5*, 1500721.
[44] J. Song, H. Lu, A. Gruverman, S. Ducharme, *Appl. Phys. Lett.* **2014**, *104*, 192901.
[45] V. W. Bergmann, S. A. Weber, F. J. Ramos, M. K. Nazeeruddin, M. Grätzel, D. Li, A. L. Domanski, I. Lieberwirth, S. Ahmad, R. Berger, *Nat. Commun.* **2014**, *5*, 5001.
[46] E. Edri, S. Kirmayer, S. Mukhopadhyay, K. Gartsman, G. Hodes, D. Cahen, *Nat. Commun.* **2014**, *5*, 3461.